ACS OMEGA

http://pubs.acs.org/journal/acsodf

Article

Kinetics, Thermodynamics, and Mechanism of Cu(II) Ion Sorption by Biogenic Iron Precipitate: Using the Lens of Wastewater Treatment to Diagnose a Typical Biohydrometallurgical Problem

Babatunde Oladipo, Elaine Govender-Opitz, and Tunde V. Ojumu*

Cite This: *ACS Omega* 2021, 6, 27984−27993

Read Online

ACCESS | Metrics & More | Article Recommendations | Supporting Information

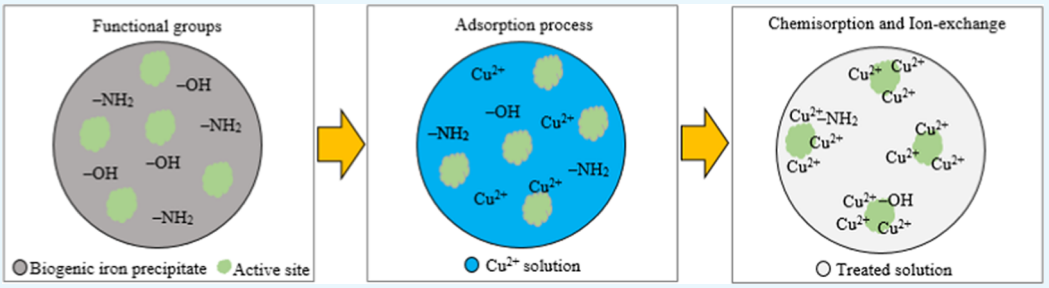

ABSTRACT: The feasibility of improving typical biohydrometallurgical operation to minimize copper losses was investigated by the use of biogenic iron precipitate for the uptake of Cu(II) ions from aqueous solutions. The iron precipitate was obtained from mineral sulfide bioleaching and characterized using SEM/EDS, XRD, FTIR, BET, TGA, and pH_{pzc} analyses. The results show that the precipitate is highly heterogeneous and that Cu(II) ion adsorption can be described by both Freundlich and Langmuir adsorption isotherms, with a maximum adsorption capacity of 7.54 mg/g at 30 °C and 150 mg/L. The sorption followed pseudo-second-order kinetics, while the major presence of −OH and $-NH_2$ functional groups initiated a chemisorption mechanism through an ion-exchange pathway for the process. Ionic Cu(II) (radius (0.72 Å)) attached easily to the active sites of the precipitate than hydrated Cu(II) (radius (4.19 Å)). With an estimated activation energy of 23.57 kJ/mol, the obtained thermodynamic parameters of $\Delta S°$ (0.034−0.050 kJ/mol K), $\Delta G°$ (8.37−10.64 kJ/mol), and $\Delta H°$ (20.07−23.81 kJ/mol) indicated that the adsorption process was chemically favored, nonspontaneous, and endothermic, respectively. The 43% Cu(II) removal within 60 min equilibrium contact time at pH 5 was indicative of the reduced efficiency of copper extraction observed in a real-life biohydrometallurgical process due to sorption by the iron precipitate. The result of this study might provide an insight into the management of the biohydrometallurgical process to minimize copper losses. It may also help mitigate environmental pollution caused by the disposal of these biogenic iron precipitate residues.

1. INTRODUCTION

Extensive literature studies have shown that iron precipitation during the dissolution of sulfide minerals using hydro- and biohydrometallurgical treatment is an inevitable phenomenon.[1,2] Authors have suggested that precipitate formation serves as the outlet path for unwanted iron, alkali ions, or sulfate ions from the processing circuit.[3,4] While precipitate formation can be minimized,[5,6] significant accumulation over continuous long-term operation may lead to slow kinetics and reduce the efficiency of bioleaching processes by occluding desired metals within the precipitate residue.[1,7] In recent times, due to the absence of efficient technologies to treat these iron residues, they are stored in waste dams, occupying large acres of land.[8] This poses an environmental risk with the potential for heavy metal pollution of the soil and groundwater systems.[9]

Due to the continuous increase in industrialization and urbanization, the world's copper mining capacity has been on the increase, with approximately 20% of the global copper production through biohydrometallurgy.[10] It is well known that the production of iron precipitate is unavoidable and would continue to persist in biohyrometallurgical operations; however, there is an opportunity to harness these waste residues as a low-cost precursor for the recovery of heavy metal ions. The large surface area, enhanced porosity, and good surface chemistry and reactivity properties[11] make the precipitate a good sorption candidate for the removal of heavy metal contaminants such as copper from wastewater systems.

Received: July 20, 2021
Published: October 17, 2021

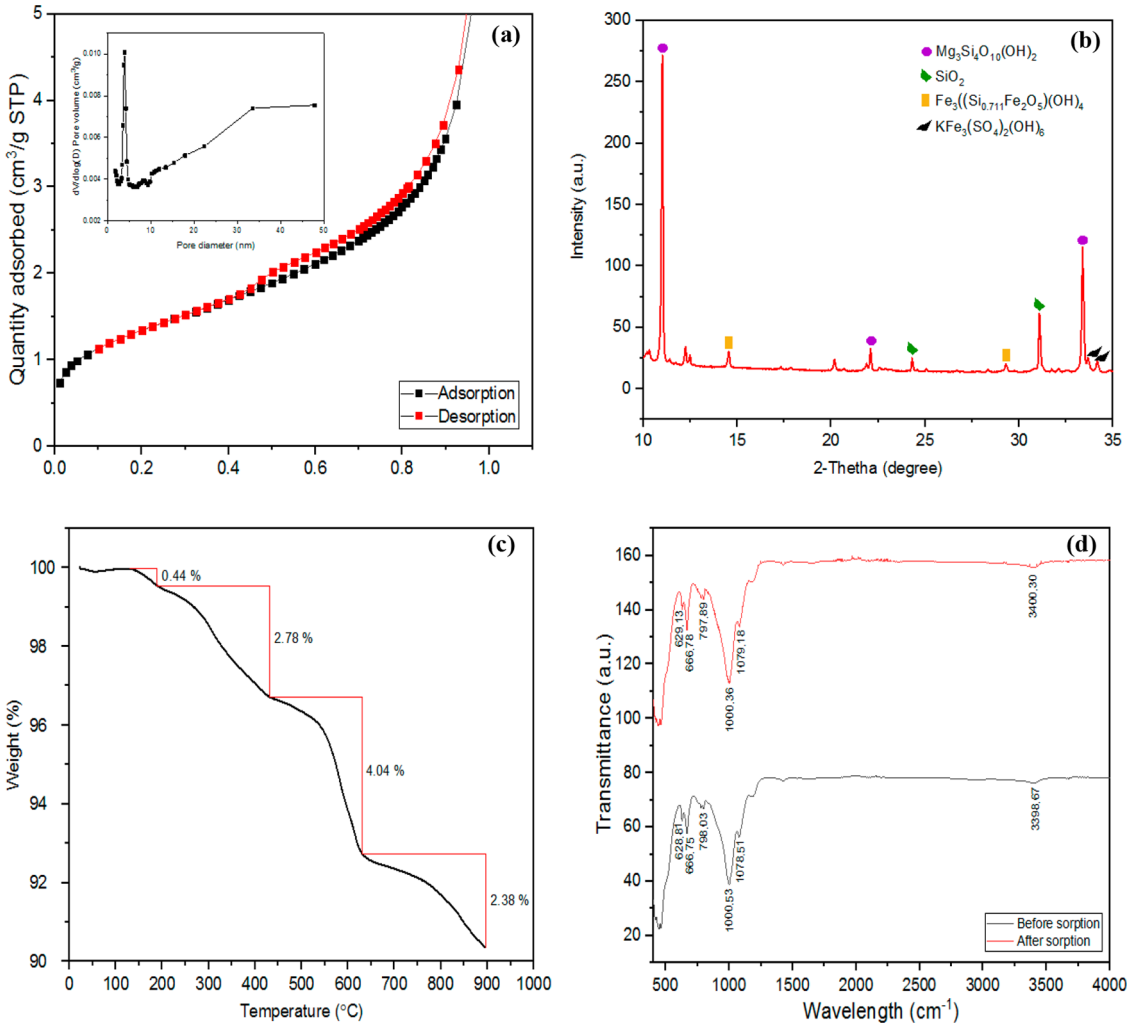

Figure 1. Plots of (a) N_2 adsorption/desorption isotherms and adsorption pore-size distribution (inset), (b) XRD pattern, (c) TGA curve, and (d) FTIR spectra of iron precipitate residue samples.

Since the toxic metals present in the iron residues have an intrinsic value, the opportunity for recovery of the desired metal will also result in the mitigation of environmental pollution. A few studies have shown the recovery of heavy metals from iron precipitate-metallurgical byproducts, such as goethite[12] and jarosite.[8,13] Ju et al.[8] reported that 97% Zn and 87% Cu could be directly recovered from jarosite waste produced during zinc hydrometallurgical operations. In the work of Liu et al.,[13] the authors found that 89.4% Fe, 80.7% Zn, 90.7% Cu, and 48.8% Cd could be recovered from jarosite using microwave-assisted sulfuric acid roasting and water leaching. In another study, Li et al.[14] reported that 95.4% In and 95.5% Cu could be extracted from zinc residue leach liquor by solvent extraction.

Although there are several studies[15−18] on sorption isotherms with respect to the use of synthesized and/or biogenic iron compounds in the treatment of wastewater systems, none investigated the nature of sorption at solid/liquid interfaces. For example, Castro et al.[18] studied heavy metal adsorption from aqueous solutions using biogenic iron compounds (mainly siderite and magnetite) obtained from a natural microbial consortium of an abandoned mine, Jaiswal et al.[16] synthesized goethite mineral as an adsorbent for the uptake of copper and cadmium from synthetic wastewater, and Dou et al.[17] experimented on the sorption of arsenate on different types of granular schwertmannite from aqueous solutions. However, the mode of sorption may provide some understanding of how biohydrometallurgical operation can be better managed at least in the context of minimizing copper losses in bioleaching operation.

This work aims to investigate the kinetics, thermodynamics, and mechanism of sorption of copper ions from wastewater by biogenic iron precipitate. The influence of several sorption factors, namely, solution pH, temperature, contact time, and initial metal ion concentration, was investigated. The view is to provide an understanding of the sorption mode that may be explored to improve and manage a typical biohydrometallurgical operation more efficiently. The result may also help to reduce environmental pollution caused by biogenic iron precipitate residues disposal.

2. RESULTS AND DISCUSSION

2.1. Analyses of the Iron Precipitate. The procured iron precipitate residue was characterized by FTIR, SEM/EDX, XRD, TGA, and BET analyses to demonstrate its adsorption capacity for Cu(II) in an aqueous solution.

The N_2 adsorption−desorption isotherm of the sample is depicted in Figure 1a.

https://doi.org/10.1021/acsomega.1c03855
ACS Omega 2021, 6, 27984−27993

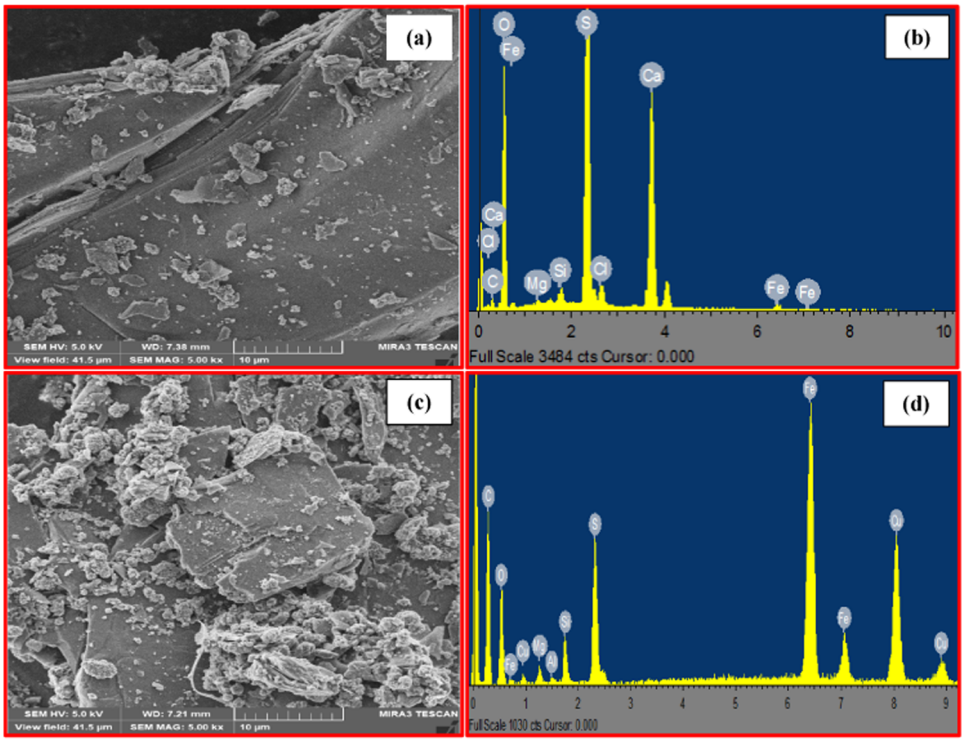

Figure 2. (a) SEM image before Cu(II) adsorption, (b) EDS image before Cu(II) adsorption, (c) SEM image after Cu(II) adsorption, and (d) EDS image after Cu(II) adsorption on iron precipitate residue powder.

The plot displays the principal type-IV pattern and hysteresis loop type,[19] signifying that the powdered residue is mesoporous. The BET surface area and BJH pore volume of the sample were evaluated to be 4.74 m^2/g and 0.014 cm^3/g, respectively, whereas the average pore diameter value was determined to be 11.61 nm. In comparison with the iron precipitate powder used in this study, Cu(II) ion has an ionic diameter of 0.072 nm (0.72 Å),[20] indicating that Cu(II) ions could easily be adsorbed by ion exchange onto the pores of the adsorbent in a given pore volume. In the context of physisorption, pore size between 2 and 50 nm is referred to as mesopore.[19] Based on the adsorption pore-size distribution curve (Figure 1a (inset)), it was observed that most of the average pore sizes range between 2 and 15 nm, which confirmed that the powdered iron precipitate is majorly mesopores. This suggests there would be easy access for Cu(II) ions to adsorb into the active sites of the adsorbent due to favorable surface area and pore size.

The XRD pattern of the iron precipitate powder is depicted in Figure 1b. The result revealed that the powdered sample is heterogeneous in composition and mainly dominated by talc. Other phases identified are quartz, cronstedtite, and potassium jarosite. The peaks at 2θ = 11, 23, and 33° were assigned to the characteristic peaks of talc ($Mg_3Si_4O_{10}(OH)_2$) with an average crystallite size of 290 nm. The peaks at 2θ = 24 and 31° corresponded to the characteristic peaks of quartz (SiO_2) with an average crystallite size of 284 nm. The appearance of peaks at 2θ = 14 and 29° was indexed to the peculiar peaks of cronstedtite ($Fe_3((Si_{0.711}Fe_{0.289})_2O_5)(OH)_4$) with an average crystallite size of 172 nm. The peaks identified at 2θ = 33 and 34° were ascribed to the characteristic peaks of potassium jarosite ($KFe_3(SO_4)_2(OH)_6$) with an average crystallite size of 143 nm. The major presence of talc is an indication of the high surface area and ion-exchange properties of the biogenic iron precipitate.

The thermal behavior of iron precipitate residue powder was checked with the TGA curve, as displayed in Figure 1c. The plot revealed four distinct weight loss phases. Noticeable at 180 and 425 °C were the first two-weight losses of 0.44 and 2.78%, respectively, which can be ascribed to the loss of physically adsorbed water and interlayered water within the lattice crystals, respectively. Mass loss of $Fe_3((Si_{0.711}Fe_{0.289})_2O_5)(OH)_4$ and $KFe_3(SO_4)_2(OH)_6$ in the temperature range between 425 and 625 °C could be attributed to the likely formation of γ-Fe_2O_3 and loss of SO_2, respectively. The third mass loss of 4.04% at 625 °C was assumed to be due to the transformation of SiO_2 present in the residue sample, while the final weight loss of 2.38% was linked to the decomposition of $Mg_3Si_4O_{10}(OH)_2$ observed at >830 °C. Moreover, the loss of weight at each stage was marked by an endothermic process. The negligible mass loss observed at the high-temperature range of the TGA profile indicated that the iron precipitate powder has good thermal stability. Thus, it could be used as an adsorbent for high-temperature adsorption processes.

FTIR spectra obtained to check the qualitative attribute and modification of surface functional groups of the iron precipitate powder, before and after adsorption, are illustrated in Figure 1d. The broad peaks at 3398.67 and 3400.30 cm^{-1} before and after Cu(II) adsorption are ascribed to both the stretching vibrations of the hydroxyl (−OH) and symmetrical aliphatic amine ($-NH_2$) of polymeric compounds.[21−23] The slight shift in the wavelength of the peak after adsorption is due to the attachment of Cu^{2+} to −OH and $-NH_2$ groups. The polar functional group identified on the top layer of the iron precipitate powder facilitates chemisorption processes with cation exchange capacity. The occurrence of out-of-plane C−H

https://doi.org/10.1021/acsomega.1c03855
ACS Omega 2021, 6, 27984−27993

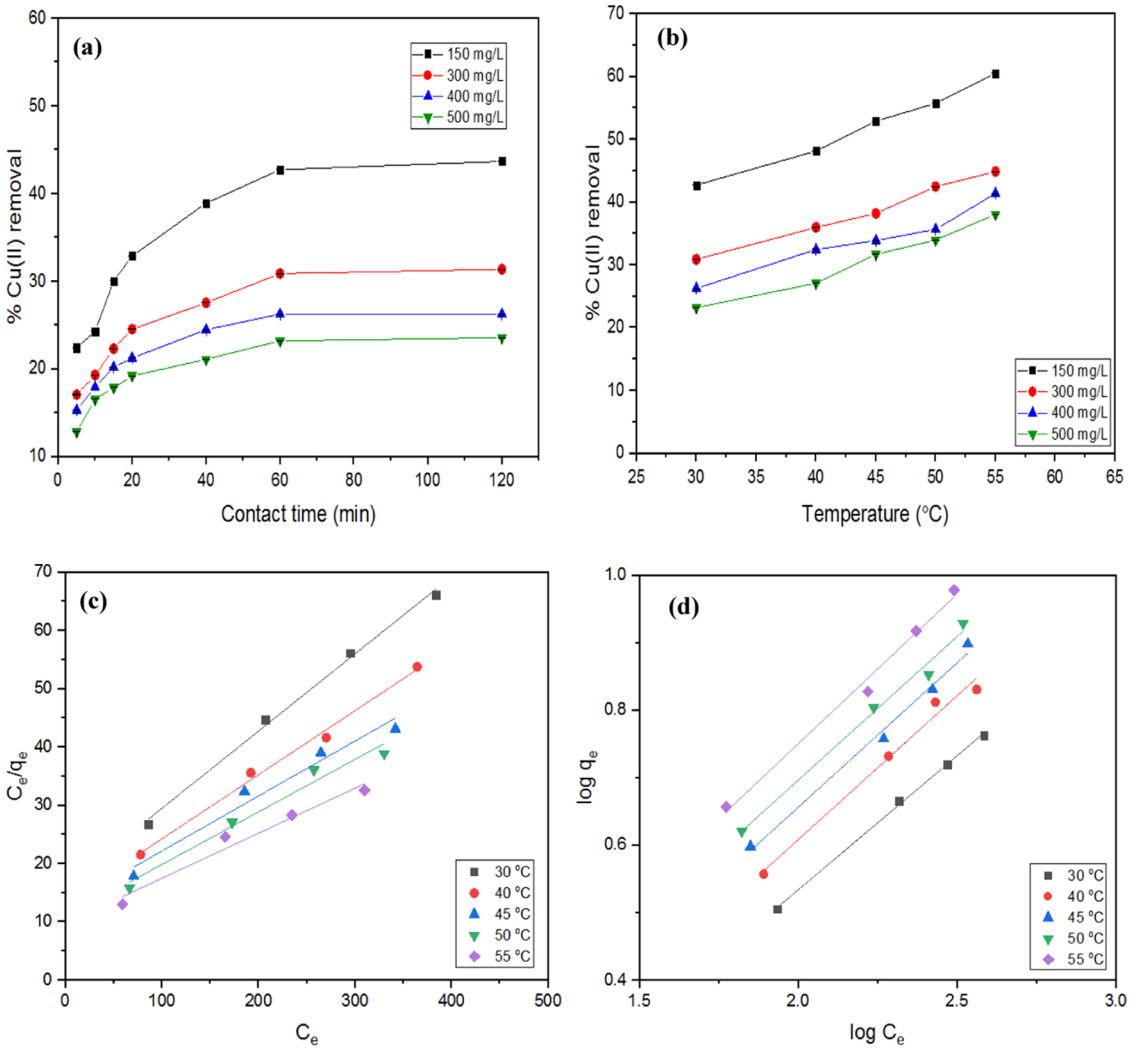

Figure 3. (a) Influence of contact time and (b) influence of temperature on percentage Cu(II) removal at various Cu(II) ion concentrations (data are expressed as the mean of three replicate ± standard deviation) and (c) Langmuir plots and (d) Freundlich isotherm plots of Cu(II) adsorption onto the iron precipitate powder at the investigated temperatures.

bending vibrations identified at 798.03 cm^{-1} indicated the presence of mononuclear aromatic hydrocarbons.[24] Before adsorption, bands detected at 1078.51 and 1000.53 cm^{-1} could both be ascribed to the stretching vibrations of silicate (SiO_4^{4-}) and phosphate (PO_4^{3-}) ions,[21] suggesting the presence of silicon and phosphorus compounds in the iron precipitate powder. A slight shift was observed in these bands after adsorption. Bands present in the region of 666.75−628.81 cm^{-1} before Cu(II) adsorption were ascribed to the presence of sulfate ions (SO_4^{2-}) of sulfur functional groups or alkyne C−H bending vibration of alkyne groups.[21,23] FTIR spectra of the samples showed either a slight increase or a reduction in the wavelength of sorption peaks after adsorption, which indicates that an ion-exchange mechanism could be the sorption pathway for the uptake of Cu(II). Besides, the major presence of negatively charged ionizable functional groups of hydroxyl (−OH) and amino ($-NH_2$) located on the surface of the adsorbent have a great ability to interact with a proton or metal ion,[25] whereby a covalent chemical bond is established via the interaction of the adsorbed Cu(II) ions with the adsorbent.

The sites accountable for the adsorption process can be expressed as shown in eqs 1 and 2

$$S - OH + M^{n+} \rightarrow S - OM^{(n-1)+} + H^+ \quad (1)$$

$$S - NH_2 + M^{n+} \rightarrow S - NM^{(n-2)+} + 2H^+ \quad (2)$$

where S represents the surface of the adsorbent.

The SEM/EDS surface morphology and identified elements on the iron precipitate powder before and after adsorption are displayed in Figure 2.

Observed in the SEM image before adsorption (Figure 2a) is a smooth surface with noticeable scattered, irregular, and elongated flat pieces compared to the SEM image after adsorption (Figure 2c). The EDS elemental composition of the sample before adsorption is shown in Figure 2b, with the presence of some metallic ions. In Figure 2c, the observed clusters of agglomerated particles on the surface of the biogenic precipitate may be attributed to agitation and random site selection during the adsorption process. The iron precipitate powder has a large surface area, primarily due to its crystalline form, which may be ascribed to its ability to entrap metallic ions. After adsorption, there was a shift in valencies of the metallic ions and the presence of Cu(II) ions could be observed on the surface (Figure 2d), indicating the feasibility of the iron precipitate to adsorb metals. The

https://doi.org/10.1021/acsomega.1c03855
ACS Omega 2021, 6, 27984−27993

percentage elemental composition before and after copper adsorption is displayed in Table S1 of the Supporting Information (SI).

2.2. Study of Adsorption Factors. Adsorption factors, namely initial solution pH, adsorption time, initial Cu(II) concentrations, and solution temperatures, as they influenced the batch adsorption process in this study, are discussed below.

The impact of initial Cu(II) concentration on the sorption capacity of the iron precipitate powder was investigated for adsorption time values from 5 to 120 min and concentration values of 150−500 mg/L at 30 °C solution temperature, pH 5, 150 rpm agitation speed, and 1 g dosage of the iron precipitate powder. As presented in Figure 3a, the increase in the initial Cu(II) concentration from 150 to 500 mg/L led to (i) an increase in the adsorption capacity from 3.20 to 5.80 mg/g and (ii) a decrease in the adsorption rate and removal Cu(II) efficiency from 42.73 to 23.20%. These observations suggest that at lower concentrations, Cu(II) ions in the reaction system experience higher interaction with the top layer of the adsorbent due to the large ratio of unoccupied sorption sites to initial Cu(II) concentration. In contrast, the ratio of available sites for Cu(II) ions decreases at higher concentrations due to saturation of the binding sites.

The relationship between the adsorption of Cu(II) onto the surface of the iron precipitate and contact time is presented in Figure 3a. It was observed that the adsorption capacity and percentage removal of the adsorbent increase as the contact time increases, after which equilibrium was attained at 60 min. Beyond this equilibrium point, the adsorption capacity of the iron precipitate was in dynamic equilibrium with the adsorbed quantity of Cu(II), as indicated by an insignificant increase in the percentage Cu(II) uptake after 60 min. The percentage removal of Cu(II) was rapid at the beginning of the adsorption process (Figure 3a) due to the available rich active sites of the adsorbent and the small diameter of the Cu(II) ion. After 60 min, the Cu(II) ions could not easily penetrate the inner pores of the adsorbent, which is assumed to be linked to Cu(II) monomolecular saturation of the surface pores, as shown in the SEM image after adsorption (Figure 2c). The results from Figure 3a further demonstrate that the equilibrium time was independent of the initial Cu(II) concentration.

The influence of temperature on the sorption capacity of the iron precipitate was examined for temperature values between 30 and 55 °C at pH 5, 150 mg/L initial Cu(II) concentration, 150 rpm agitation speed, 1 g adsorbent dosage, and 60 min contact time. As shown in Figure 3b, Cu(II) adsorption onto the iron precipitate powder is considerably affected by temperature over the range of Cu(II) ion concentrations under investigation in this study. As observed for the test with an initial Cu(II) concentration of 150 mg/L, the adsorption efficiency increased from 42.73 to 60.51% with an increase in temperature from 30 to 55 °C. This indicates that higher temperatures enhanced the adsorption process for metal ion binding, suggesting that Cu(II) adsorption by the iron precipitate is an endothermic process. Furthermore, increasing the temperature could lead to an expansion in the pore size of the adsorbent, which helps to ease the diffusion of Cu(II) ions onto the sites difficult to access.

The pH of the solution governs the sorption affinity of the adsorbent by influencing the type of charge on the surface of the adsorbent, speciation of the metal in the solution, and ionizing strength of the adsorbent. In this study, pH-dependent experimental runs were not conducted at pH values >5 to prevent Cu(II) precipitating as insoluble copper hydroxide, which can hinder true adsorption studies. The influence of pH could also be described through the point of zero charge (pH_{pzc}). pH_{pzc} refers to the pH at which the surface of the adsorbent has a net charge of zero. The value of pH_{pzc} obtained in this study is 4.02 (Figure S1 of the SI). This suggests that the surface of the adsorbent is positively charged and favors sorption of anions for solution pHs < pH_{pzc} (4.02), while it becomes negatively charged to favor sorption of cations for solution pHs > pH_{pzc} (4.02). This property of the adsorbent further supports the finding that optimum Cu(II) adsorption onto the iron precipitate powder takes place at pH 5 (>pH_{pzc}), under which conditions the surface of the adsorbent is negatively charged.

2.3. Adsorption Isotherms. Adsorption isotherms are useful in explaining the interaction between the adsorbate and the adsorbent and in defining optimal adsorbent application.[26] The influence of temperature on the equilibrium capacity of the iron precipitate powder for Cu(II) ions uptake was determined using well-established isotherm models, viz., the Langmuir and Freundlich models. The goodness of fit of the applied models to experimental data was checked by the coefficient of determination (R^2).

The Langmuir isotherm model is valid for monolayer adsorption of solutes at definite homogeneous sites on the surface layer of the adsorbent, with no more than one adsorbate molecule occupying a site.[27] The linearized form of the model is expressed in eq 3

$$\frac{C_e}{q_e} = \frac{1}{q_m b} + \frac{C_e}{q_m} \quad (3)$$

where q_e is the equilibrium quantity of Cu(II) adsorbed onto the iron precipitate powder (mg/g), C_e denotes the equilibrium Cu(II) concentration in the solution (mg/L), q_m denotes the maximum adsorption capacity (mg/g), and b represents the Langmuir constant associated with Cu(II) ion affinity for adsorption sites and energy (L/mg). The linear plots of C_e/q_e versus C_e are depicted in Figure 3c, and the estimated constants of the equation are displayed in Table S2 of the SI. High values of R^2 obtained were within the range of 0.965−0.996, with the R^2 value obtained at 303 K to be 0.996. The high R^2 values suggest that the model predictions are accurate within the variance of the experimental data. The Langmuir maximum adsorption capacity of 7.54 mg/g was obtained at 30 °C, 150 mg/L, 1 g adsorbent dosage, and pH 5 within 60 min. It was also observed that the values of q_m increase with increasing temperature, signifying that Cu(II) adsorption by the iron precipitate powder is indeed an endothermic process. The results and details of the separation factor (R_L), which is an important feature of the Langmuir isotherm, are given in Table S2 and Text S1 of the SI, respectively.

Table 1 shows a comparison of the maximum adsorption capacity (q_m) of various untreated adsorbents for Cu(II) removal from aqueous solutions. The comparatively high maximum adsorption capacity of the iron precipitate used in this study suggests that this is a competitive recovery technology to existing processes used for Cu(II) uptake from polluted water.

The Freundlich isotherm model holds for multilayer adsorption of solutes onto a heterogeneous adsorbent surface

https://doi.org/10.1021/acsomega.1c03855
ACS Omega 2021, 6, 27984−27993

Table 1. Langmuir Maximum Adsorption Capacity, q_m (mg/g), of Various Untreated Waste Adsorbents for Cu(II) Removal

adsorbent	q_m (mg/g)	references
tree barks	7.00	Martin-Dupont et al.[28]
banana peel	4.75	Kurniawan et al.[29]
pomegranate peel	1.32	El-Ashtoukhy et al.[30]
rice shell	2.95	Aydın et al.[31]
barley straws	4.64	Pehlivan et al.[32]
Uncaria gambir	9.95	Tong et al.[33]
natural spider silks	3.27	Pelit et al.[34]
kolubara lignite	4.05	Milicevic et al.[35]
litchi pericarp	8.83	Kong et al.[36]
iron precipitate	7.54	this study

with nonuniform adsorption sites.[37] The linearized form for this isotherm model is represented in eq 4

$$\log q_e = \log K_f + \frac{1}{n_f}\log C_e \quad (4)$$

where n_f and K_f represent the heterogeneity factor and Freundlich constant in relation to the adsorption intensity and adsorption capacity, respectively. The linear plots of log q_e versus log C_e are depicted in Figure 3d. Very high R^2 values within the range of 0.991−0.999 were estimated, with the R^2 value obtained at 303 K to be 0.999. These values are listed in Table S3 of the SI, which also provides the model correlations for n_f and K_f at each temperature investigated. The increase in K_f values with increasing temperature also demonstrates the endothermic nature of the Cu(II) adsorption process. The values and implication of n_f, which indicates the feasibility of the adsorption process, are given in Table S3 and Text S2 of the SI, respectively.

Based on the comparison of R^2 values, both Langmuir and Freundlich models fit well with the experimental data. The very high R^2 values obtained according to the Freundlich model indicate that the iron precipitate powder is highly heterogeneous, which is corroborated by the XRD analysis of the sample. It further suggests that, at high Cu(II) concentrations, adsorption probably occurs on the multilayer surface of the iron precipitate.

2.4. Adsorption Kinetics and Model Fitting. Adsorption kinetics describe the rate of solute uptake at the solid−liquid boundary and gives important data on the equilibrium time, which is integral for the design and operation of an adsorption process.[26] The kinetics of Cu(II) adsorption by the iron precipitate powder was investigated with the pseudo-first-order, pseudo-second-order, and Elovich kinetic models.

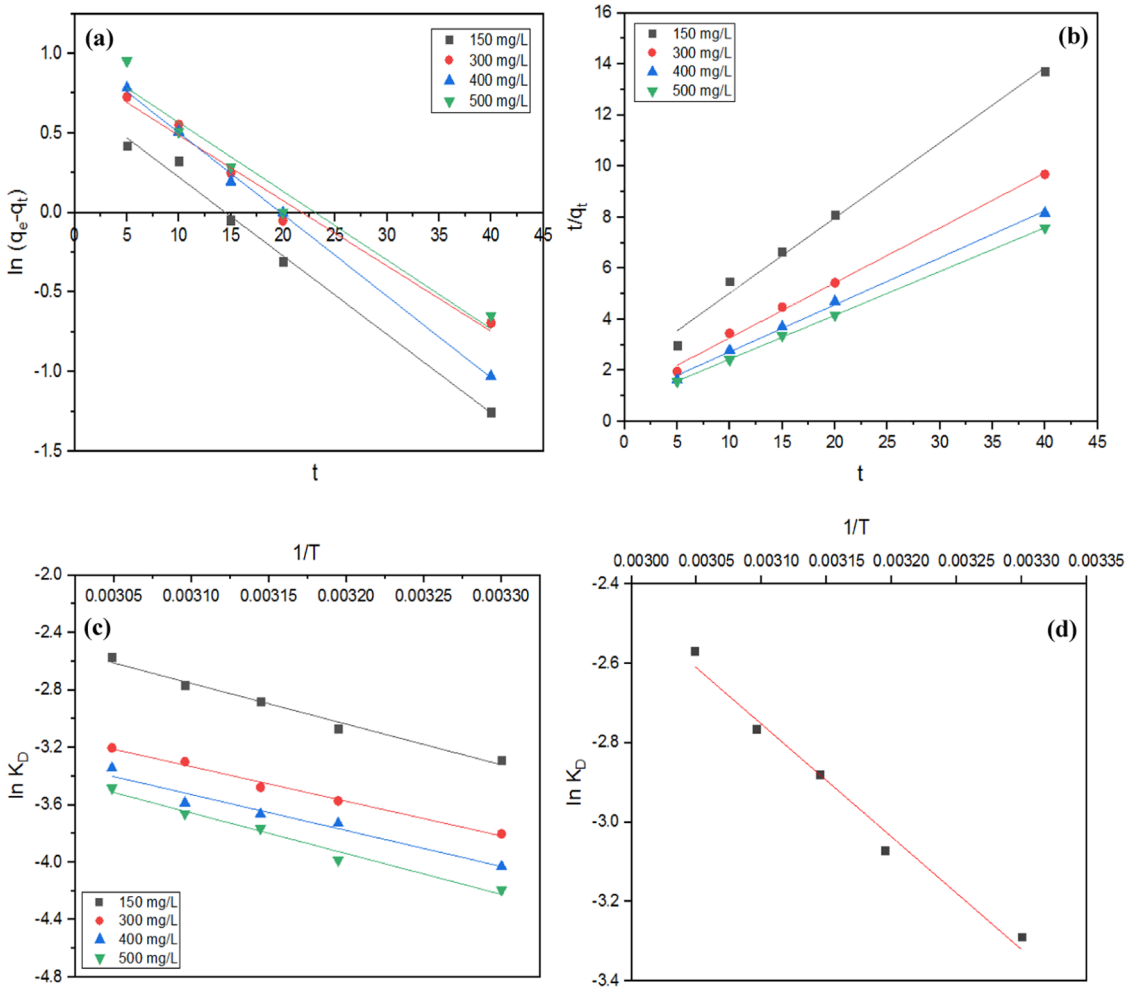

Figure 4. (a) Pseudo-first-order kinetic plots and (b) pseudo-second-order kinetic plots at the studied Cu(II) concentrations, (c) van't Hoff plots at various Cu(II) concentrations, and (d) Arrhenius plot at 303−328 K and 150 mg/L for Cu(II) adsorption onto the iron precipitate powder.

https://doi.org/10.1021/acsomega.1c03855
ACS Omega 2021, 6, 27984−27993

Table 2. Kinetic Parameters and Model Correlations for Cu(II) Adsorption onto the Iron Precipitate Powder at the Studied Initial Cu(II) Concentrations

		pseudo-first-order			pseudo-second-order			Elovich		
C_0 (mg/L)	$q_{e,exp}$ (mg/g)	$q_{e,cal}$ (mg/g)	k_1 (min^{-1})	R^2	$q_{e,cal}$ (mg/g)	k_2 (g/mg min)	R^2	β (g/mg)	α (mg/g min)	R^2
150	3.205	2.049	0.049	0.992	3.392	0.042	0.990	1.591	1.523	0.952
300	4.633	2.454	0.041	0.980	4.640	0.041	0.997	1.261	3.662	0.978
400	5.252	2.765	0.051	0.998	5.429	0.038	0.998	1.123	5.355	0.997
500	5.800	2.717	0.043	0.957	5.821	0.041	0.999	1.006	5.677	0.978

Table 3. Thermodynamic Parameters for Cu(II) Adsorption onto the Iron Precipitate Powder[a]

			ΔG (kJ/mol) at investigated temperatures				
initial Cu(II) concentrations (mg/L)	ΔH (kJ/mol)	ΔS (kJ/mol K)	303 K	313 K	318 K	323 K	328 K
150	23.57	0.050	8.37	7.87	7.61	7.36	7.11
300	20.07	0.034	9.61	9.27	9.10	8.92	8.75
400	23.81	0.044	10.33	9.88	9.66	9.44	9.22
500	23.59	0.043	10.64	10.21	10.00	9.79	9.57

[a]ΔH (kJ/mol) is the enthalpy change, ΔS (kJ/mol K) is the entropy change, and ΔG (kJ/mol) is the Gibbs free energy change.

The pseudo-first-order model was established on the adsorbent capacity. It describes the rate of change in adsorbate uptake with time to be directly proportional to the difference in saturation concentration levels. The linearized form of the equation is expressed in eq 5[38]

$$\ln(q_e - q_t) = \ln q_e - k_1 t \quad (5)$$

where q_e and q_t are the quantities of Cu(II) adsorbed (mg/g) at equilibrium and at time t (min), respectively, and k_1 represents the pseudo-first-order rate constant (min^{-1}). The linear plots of $\ln(q_e - q_t)$ versus t are depicted in Figure 4a.

The estimated model parameters at the studied conditions are summarized in Table 2. Although the fitted model gave high R^2 values between 0.957 and 0.998, the calculated $q_{e,cal}$ values of the model differs greatly from the experimental $q_{e,exp}$ values at initial Cu(II) concentrations. This deviation indicates that the pseudo-first-order equation may not adequately explain the adsorption pathway of Cu(II) onto the surface of the iron precipitate powder, which suggests the need to assess the efficacy of another kinetic model.

The pseudo-second-order model can adequately describe adsorption kinetic experimental data. It describes the rate of occupation of adsorption sites to be proportional to the square of the number of unoccupied sites. The linearized form of the model is given in eq 6[39]

$$\frac{t}{q_t} = \frac{1}{k_2 q_e^2} + \frac{t}{q_e} \quad (6)$$

where q_e and q_t are the quantities of Cu(II) adsorbed (mg/g) at equilibrium and at time t (min), respectively, and k_2 represents the equilibrium pseudo-second-order rate constant (g/mg min).

The linear plots of t/q_t versus t are shown in Figure 4b. The very high R^2 values obtained were in the range of 0.990−0.999, with the calculated model parameters presented in Table 2. The results indicate a better fit with the pseudo-second-order equation than the pseudo-first-order model. This may be observed by the negligible differences between the model estimated $q_{e,cal}$ values and the experimental $q_{e,exp}$ values for the initial Cu(II) concentrations being studied. Thus, the pseudo-second-order model being the best fit suggests that both the concentration of Cu(II) in solution and the amount of available active sites on the iron precipitate powder can be used to mathematically describe the intrinsic kinetic adsorption constant.[40,41]

Elovich's equation describes the kinetics of chemical adsorption systems. The model is very applicable to a profound heterogeneous system. The linearized expression for the Elovich model is shown in eq 7[42]

$$q_t = \frac{1}{\beta}\ln \alpha\beta + \frac{1}{\beta}\ln t \quad (7)$$

where q_t denotes the amount of Cu(II) adsorbed (mg/g) onto the iron precipitate powder at time t, α represents the initial Cu(II) adsorption rate (mg/g min), and β represents the degree of activation energy and surface coverage for chemisorption (g/mg). The plots of q_t versus $\ln t$ for Cu(II) removal by the iron precipitate powder applied to the Elovich equation are displayed in Figure S2 of the SI, and the estimated constants of the equation are presented in Table 2. The high coefficient of determination values obtained for the Elovich model signifies the involvement of the chemisorption mechanism in the system, which may involve valence forces via the sharing or exchange of electrons between Cu(II) ions and the iron precipitate powder. The expected interactions with the −OH and $-NH_2$ functional groups further validates the FTIR results, suggesting that the ion-exchange mechanism also plays a vital part in the adsorption process.

2.5. Thermodynamic and Activation Energy Parameters. Evaluation of thermodynamic parameters helps in predicting the feasibility and mechanism of an adsorption system. After adsorption equilibrium of the studied systems was established, thermodynamic data, namely, $\Delta G°$, $\Delta S°$, and $\Delta H°$, were evaluated for Cu(II) adsorption onto the iron precipitate powder according to eqs 8−10

$$\Delta G° = -RT \ln K_D \quad (8)$$

The standard thermodynamic distribution coefficient (K_D)[41,43] was calculated at different temperatures and initial Cu(II) concentrations.

$$K_D = \frac{q_e}{C_e} \quad (9)$$

https://doi.org/10.1021/acsomega.1c03855
ACS Omega 2021, 6, 27984−27993

where q_e, the equilibrium quantity, and C_e, the equilibrium concentration, have been defined previously in eq 3

$$\ln K_D = \frac{\Delta S^\circ}{R} - \frac{\Delta H^\circ}{RT} \quad (10)$$

where R (8.314 J/mol K) represents the gas constant and T (K) represents the absolute solution temperature. Based on eq 10, the respective values of ΔH° and ΔS° were estimated from the slope and intercept of linear van't Hoff plots of $\ln K_D$ versus $1/T$ (Figure 4c). A summary of the model predictions for ΔH°, ΔS°, and ΔG° are provided in Table 3.

The positive values of ΔH° further support the finding that the adsorption process is endothermic, which is unequivocally attributable to chemisorption. The positive values of ΔS° demonstrate increased dissociation and randomness at the solid/liquid boundary during the adsorption process. This suggests that Cu(II) ions replaced some water molecules in the solution earlier adsorbed on the surface of the adsorbent. Likewise, positive values of ΔG° are an indication of the nonspontaneity and ion exchange process in the adsorption system. This suggests that energy and agitation are required for the adsorption process to be carried out in this study. The decrease in ΔG° values observed as the temperature increases shows that a higher sorption rate occurred at elevated temperatures.

Activation energy allows the determination of the energetic barrier that Cu(II) ions must overcome before being attached to the adsorption sites. The activation energy was determined using the linearized form of the Arrhenius equation as expressed in eq 11

$$\ln K_D = \ln A - \left(\frac{E_a}{R}\right)\frac{1}{T} \quad (11)$$

where E_a (kJ/mol) is the activation energy, K_D represents the equilibrium rate constant, A is the Arrhenius constant, R (8.314 J/mol K) represents the gas constant, and T (K) is the absolute solution temperature. Based on eq 11, the value of E_a was estimated from the slope of the plot of $\ln K_D$ versus $1/T$ (Figure 4d) at 303−328 K and 150 mg/L. The type of adsorption can be determined by the magnitude of the activation energy. A chemical adsorption process has an activation energy in the range of 4−40 kJ/mol.[44] In this study, the activation energy was evaluated to be 23.57 kJ/mol, indicating a chemical adsorption process. The Arrhenius expression obtained in this study is given in Text S3 of the SI.

2.6. Implications of Cu(II) Adsorption in Biohydrometallurgical Processes. It has been demonstrated in this study that biogenic iron precipitate adsorbs Cu(II) ions via combined mechanisms of chemisorption and ion exchange, with the adsorption process requiring an estimated activation energy of 23.57 kJ/mol. In the bioleaching of low-grade copper sulfide, such as chalcopyrite, high-temperature (60−80 °C) operation promotes rapid adsorption of copper onto the iron precipitate, thereby preventing the release of the entrapped copper into the solution for further processing.[45,46] In this study, it has been shown that during Cu(II) adsorption onto the iron precipitate, there appears to be competition for the active sites between the ionic Cu(II) (radius (0.72 Å)) and the hydrated Cu(II) (radius (4.19 Å)),[20] with the former easily adsorbed onto the pores of the biogenic precipitate due to its smaller radius. This entrapment of copper during the high-temperature dissolution of copper-bearing chalcopyrite mineral is expected to affect the overall extraction and recovery of the process. Given that operating conditions (such as pH and temperature) have been shown to affect the particle size of iron precipitate,[47] it may also be possible to adjust the process conditions in bioleaching operations, such that the pore size of the particle becomes smaller for Cu(II) ions to be entrapped. Thus, this could provide a better route for increasing copper extraction in biohydrometallurgical processes.

3. CONCLUSIONS

The intrinsic mechanism of biogenic iron precipitate entrapment of desired metals produced during biohydrometallurgical operation was unraveled in this study through the lens of its sorption in the removal of Cu(II) from aqueous solutions. Analyses of the iron precipitate sample showed that it is highly heterogeneous in terms of composition, has a large surface area, and possesses negatively charged functional groups for the uptake of Cu(II), demonstrating a chemisorption process via an ion-exchange mechanism. The pseudo-second-order model best fits the experimental data, signifying its high precision to describe the kinetic constant for Cu(II) adsorption onto the biogenic iron precipitate. Thermodynamics parameters showed that the process is nonspontaneous and endothermic. More importantly, the lessons gleaned from this study provide new insights into the rationale for the management of a typical biohydrometallurgical operation to minimize copper losses for efficient mineral processing. On the other hand, the results would help reduce land and water pollution caused by the disposal of iron precipitate residues.

4. MATERIALS AND METHODS

4.1. Iron Precipitate Residue Preparation. The iron precipitate residue was obtained from a pilot plant used for bioleaching of the pyrite concentrate using mixed mesophilic cultures. The residue was dried in a temperature-controlled Labcon incubator with a shaker (Labcon 5081U) at 80 °C for 18 h to ensure a constant weight. The oven-dried powder was then preserved in a desiccator for further use. The iron precipitate residue was utilized with no physical or chemical modification.

The pH at point of zero charge (pH_{pzc}) experiments were performed, and the details are shown in Text S4 of the SI.

4.2. Iron Precipitate Residue Characterization. Surface morphology images of the residue sample of the iron precipitate were taken with a Tescan MIRA3 RISE scanning electron microscope (SEM). Fourier transform infrared (FTIR) spectra of the samples were determined with a PerkinElmer UATR Two spectrophotometer (Llantrisant, U.K.) and recorded over the range of 4000 and 400 cm^{-1} to analyze the functional groups present. Energy-dispersive X-ray (EDS) analysis of the samples was performed to determine its elemental composition using a Thermo Fisher Nova Nano-SEM at 20 kV, and the patterns were recorded with an Oxford X-Max 20 mm^2 detector (Oxfordshire, U.K.). X-ray powder diffraction (XRD) measurements for phase identification were performed on a Bruker D8-Advance powder diffractometer, employing Cu Kα (λ = 1.5406 Å) radiation within a 2θ band of 4−60° at 2° min^{-1} scanning speed, 40 kV speed voltage, and a current of 15 mA. The surface area and pore analysis for the iron precipitate powder was determined using N_2 adsorption−desorption isotherms at −195.8 °C bath temperature with a TriStar II 3020 (Micromeritics Corp.) surface analyzer

https://doi.org/10.1021/acsomega.1c03855
ACS Omega 2021, 6, 27984−27993

equipment. The specific surface area was determined with the Brunauer–Emmett–Teller (BET) method, while the pore diameter and pore size distribution were measured using the Barrett–Joyner–Halenda (BJH) technique. Thermogravimetric analysis (TGA) for temperature behavior of the iron precipitate powder was carried out using an SDT 650 simultaneous thermal analyzer (TA Instruments, Inc.) at process conditions of a dry airflow rate of 50 mL/min, a heating rate of 10 °C/min, and a temperature range of 20–900 °C.

4.3. Batch Adsorption Studies. Stock solutions of 1000 mg/L of Cu(II) were prepared by dissolving predefined quantities of $CuSO_4{\cdot}5H_2O$ in Milli-Q ultrapure water with a resistivity ≥18 MΩ cm. The initial concentration ranges (150–500 mg/L) were further prepared from the stock solutions by dilution. The solution pH was adjusted with 0.1 N NaOH or 0.1 N HCl to obtain desired values. All chemicals employed were of analytical reagent grade. Laboratory experimental runs were performed in several 250 mL Erlenmeyer flasks, which were placed inside a thermostatic temperature-controlled shaker until equilibrium was attained. Working solutions of 50 mL Cu(II) at the studied initial concentrations (150, 300, 400, and 500 mg/L), contact times (5, 10, 15, 20, 40, 60, and 120 min), and sorption temperatures (30, 40, 45, 50, and 55 °C) were all investigated at pH 5, 150 rpm mixing speed, and 1 g adsorbent dosage. After equilibrium time, suspensions were passed through a 0.45 μm syringe filter. The concentrations of Cu(II) were determined calorimetrically on a CE 2021 UV/vis spectrophotometer (2000 series). The percentage removal of Cu(II) ($\%R_{Cu}$) in solution was estimated below (eq 12)

$$\%R_{Cu} = \frac{C_i - C_e}{C_i} \times 100 \tag{12}$$

where C_i denotes the initial Cu(II) concentration (mg/L) and C_e represents the equilibrium Cu(II) concentration (mg/L) in solution. The amount of Cu(II) adsorbed onto the iron precipitate powder at equilibrium, q_e (mg/g), was determined below (eq 13)

$$q_e = \frac{(C_i - C_e)V}{m} \tag{13}$$

where m (g) is the mass of dried iron precipitate residue and V (L) is the working solution volume. For the validity of data results, adsorption experiments were performed three times and mean values were recorded.

The adsorption kinetics, isotherms, and thermodynamics of this study are described in Text S5 of the SI.

■ ASSOCIATED CONTENT

Supporting Information

The Supporting Information is available free of charge at https://pubs.acs.org/doi/10.1021/acsomega.1c03855.

Experimental details and plot of pH at point of zero charge (pH_{pzc}) for the iron precipitate powder; adsorption kinetics, isotherms, and thermodynamics procedure; Elovich model kinetic plot; Langmuir and Freundlich isotherm model correlations for Cu(II) adsorption; Arrhenius expression; and EDS composition of the iron precipitate powder before and after Cu(II) adsorption (PDF)

■ AUTHOR INFORMATION

Corresponding Author

Tunde V. Ojumu − *Department of Chemical Engineering, Cape Peninsula University of Technology, Cape Town 7535, South Africa;* orcid.org/0000-0002-5245-0770; Phone: +27733216797; Email: ojumut@cput.ac.za

Authors

Babatunde Oladipo − *Department of Chemical Engineering, Cape Peninsula University of Technology, Cape Town 7535, South Africa*

Elaine Govender-Opitz − *Department of Chemical Engineering, University of Cape Town, Cape Town 7700, South Africa*

Complete contact information is available at: https://pubs.acs.org/10.1021/acsomega.1c03855

Notes

The authors declare no competing financial interest.

■ ACKNOWLEDGMENTS

This research was supported by the National Research Foundation, South Africa [NRF 113844]. B.O. also thanks the Centre for Postgraduate Studies (CPGS) of Cape Peninsula University of Technology (CPUT), South Africa for the postgraduate bursary provided.

■ REFERENCES

(1) Nurmi, P.; Özkaya, B.; Sasaki, K.; Kaksonen, A. H.; Riekkola-Vanhanen, M.; Tuovinen, O. H.; Puhakka, J. A. Biooxidation and precipitation for iron and sulfate removal from heap bioleaching effluent streams. *Hydrometallurgy* **2010**, *101*, 7–14.

(2) Qiu, M.-q.; Xiong, S.-y.; Zhang, W.-m.; Wang, G.-x. A comparison of bioleaching of chalcopyrite using pure culture or a mixed culture. *Miner. Eng.* **2005**, *18*, 987–990.

(3) Dutrizac, J. E.; Jambor, J. L. Jarosites and their application in hydrometallurgy. *Rev. Mineral. Geochem.* **2000**, *40*, 405–452.

(4) Malenga, E. N.; Mulaba-Bafubiandi, A.; Nheta, W. Alkaline leaching of nickel bearing ammonium jarosite precipitate using KOH, NaOH and NH_4OH in the presence of EDTA and Na_2S. *Hydrometallurgy* **2015**, *155*, 69–78.

(5) van Hille, R. P.; van Zyl, A. W.; Spurr, N. R.; Harrison, S. T. Investigating heap bioleaching: Effect of feed iron concentration on bioleaching performance. *Miner. Eng.* **2010**, *23*, 518–525.

(6) Wu, Z.-l.; Zou, L.-c.; Chen, J.-h.; Lai, X.-k.; Zhu, Y.-g. Column bioleaching characteristic of copper and iron from Zijinshan sulfide ores by acid mine drainage. *Int. J. Miner. Process.* **2016**, *149*, 18–24.

(7) Deveci, H.; Akcil, A.; Alp, I. Bioleaching of complex zinc sulphides using mesophilic and thermophilic bacteria: comparative importance of pH and iron. *Hydrometallurgy* **2004**, *73*, 293–303.

(8) Ju, S.; Zhang, Y.; Zhang, Y.; Xue, P.; Wang, Y. Clean hydrometallurgical route to recover zinc, silver, lead, copper, cadmium and iron from hazardous jarosite residues produced during zinc hydrometallurgy. *J. Hazard. Mater.* **2011**, *192*, 554–558.

(9) Oladipo, B.; Akintunde, A. M.; Ajala, S. O.; Olatunji, S. O.; Falowo, O. A.; Betiku, E. Phytoextraction of Heavy Metals from Complex Industrial Waste Disposal Sites. In *Methods for Bioremediation of Water and Wastewater Pollution*; Springer, 2020; pp 341–371.

(10) Yin, S.; Wang, L.; Kabwe, E.; Chen, X.; Yan, R.; An, K.; Zhang, L.; Wu, A. Copper bioleaching in China: Review and prospect. *Minerals* **2018**, *8*, No. 32.

(11) Gramp, J. P.; Jones, F. S.; Bigham, J. M.; Tuovinen, O. H. Monovalent cation concentrations determine the types of Fe (III) hydroxysulfate precipitates formed in bioleach solutions. *Hydrometallurgy* **2008**, *94*, 29–33.

(12) Rodriguez, N. R.; Machiels, L.; Onghena, B.; Spooren, J.; Binnemans, K. Selective recovery of zinc from goethite residue in the zinc industry using deep-eutectic solvents. *RSC Adv.* **2020**, *10*, 7328−7335.
(13) Liu, C.; Ju, S.; Zhang, L.; Srinivasakannan, C.; Peng, J.; Le, T.; Guo, Z. Recovery of valuable metals from jarosite by sulphuric acid roasting using microwave and water leaching. *Can. Metall. Q.* **2017**, *56*, 1−9.
(14) Li, X.; Wei, C.; Deng, Z.; Li, C.; Fan, G.; Rong, H.; Zhang, F. Extraction and separation of indium and copper from zinc residue leach liquor by solvent extraction. *Sep. Purif. Technol.* **2015**, *156*, 348−355.
(15) Liu, H.; Lu, X.; Li, M.; Zhang, L.; Pan, C.; Zhang, R.; Li, J.; Xiang, W. Structural incorporation of manganese into goethite and its enhancement of Pb (II) adsorption. *Environ. Sci. Technol.* **2018**, *52*, 4719−4727.
(16) Jaiswal, A.; Banerjee, S.; Mani, R.; Chattopadhyaya, M. Synthesis, characterization and application of goethite mineral as an adsorbent. *J. Environ. Chem. Eng.* **2013**, *1*, 281−289.
(17) Dou, X.; Mohan, D.; Pittman, C. U., Jr. Arsenate adsorption on three types of granular schwertmannite. *Water Res.* **2013**, *47*, 2938−2948.
(18) Castro, L.; Blázquez, M. L.; González, F.; Muñoz, J. A.; Ballester, A. Heavy metal adsorption using biogenic iron compounds. *Hydrometallurgy* **2018**, *179*, 44−51.
(19) Sing, K. S. Reporting physisorption data for gas/solid systems with special reference to the determination of surface area and porosity (Recommendations 1984). *Pure Appl. Chem.* **1985**, *57*, 603−619.
(20) Tang, C.; Shu, Y.; Zhang, R.; Li, X.; Song, J.; Li, B.; Zhang, Y.; Ou, D. Comparison of the removal and adsorption mechanisms of cadmium and lead from aqueous solution by activated carbons prepared from Typha angustifolia and Salix matsudana. *RSC Adv.* **2017**, *7*, 16092−16103.
(21) Coates, J. Interpretation of Infrared Spectra, a Practical Approach. In *Encyclopedia of Analytical Chemistry*; John Wiley & Sons, 2000.
(22) Adebisi, G. A.; Chowdhury, Z. Z.; Alaba, P. A. Equilibrium, kinetic, and thermodynamic studies of lead ion and zinc ion adsorption from aqueous solution onto activated carbon prepared from palm oil mill effluent. *J. Cleaner Prod.* **2017**, *148*, 958−968.
(23) Silverstein, R. M.; Webster, F. X.; Kiemle, D. J.; Bryce, D. L. *Spectrometric Identification of Organic Compounds*; John Wiley & Sons, 2014.
(24) Abatan, O. G.; Alaba, P. A.; Oni, B. A.; Akpojevwe, K.; Efeovbokhan, V.; Abnisa, F. Performance of eggshells powder as an adsorbent for adsorption of hexavalent chromium and cadmium from wastewater. *SN Appl. Sci.* **2020**, *2*, No. 1996.
(25) Munagapati, V. S.; Yarramuthi, V.; Nadavala, S. K.; Alla, S. R.; Abburi, K. Biosorption of Cu (II), Cd (II) and Pb (II) by Acacia leucocephala bark powder: Kinetics, equilibrium and thermodynamics. *Chem. Eng. J.* **2010**, *157*, 357−365.
(26) Oladipo, B.; Ibrahim, T. H.; Ajala, S. O.; Akintunde, A. M.; Taiwo, A. E.; Betiku, E. Synthesis of Activated Carbons for Heavy Metals Removal. In *Green Adsorbents to Remove Metals, Dyes and Boron from Polluted Water*; Springer, 2021; pp 1−31.
(27) Langmuir, I. The adsorption of gases on plane surfaces of glass, mica and platinum. *J. Am. Chem. Soc.* **1918**, *40*, 1361−1403.
(28) Martin-Dupont, F.; Gloaguen, V.; Granet, R.; Guilloton, M.; Morvan, H.; Krausz, P. Heavy metal adsorption by crude coniferous barks: a modelling study. *J. Environ. Sci. Health, Part A* **2002**, *37*, 1063−1073.
(29) Kurniawan, T. A.; Chan, G. Y.; Lo, W.-h.; Babel, S. Comparisons of low-cost adsorbents for treating wastewaters laden with heavy metals. *Sci. Total Environ.* **2006**, *366*, 409−426.
(30) El-Ashtoukhy, E.-S.; Amin, N. K.; Abdelwahab, O. Removal of lead (II) and copper (II) from aqueous solution using pomegranate peel as a new adsorbent. *Desalination* **2008**, *223*, 162−173.
(31) Aydın, H.; Bulut, Y.; Yerlikaya, Ç. Removal of copper (II) from aqueous solution by adsorption onto low-cost adsorbents. *J. Environ. Manage.* **2008**, *87*, 37−45.
(32) Pehlivan, E.; Altun, T.; Parlayıcı, S. Utilization of barley straws as biosorbents for Cu^{2+} and Pb^{2+} ions. *J. Hazard. Mater.* **2009**, *164*, 982−986.
(33) Tong, K.; Kassim, M. J.; Azraa, A. Adsorption of copper ion from its aqueous solution by a novel biosorbent *Uncaria gambir*: Equilibrium, kinetics, and thermodynamic studies. *Chem. Eng. J.* **2011**, *170*, 145−153.
(34) Pelit, L.; Ertaş, F. N.; Eroğlu, A. E.; Shahwan, T.; Tural, H. Biosorption of Cu (II) and Pb (II) ions from aqueous solution by natural spider silk. *Bioresour. Technol.* **2011**, *102*, 8807−8813.
(35) Milicevic, S.; Boljanac, T.; Martinovic, S.; Vlahovic, M.; Milosevic, V.; Babic, B. Removal of copper from aqueous solutions by low cost adsorbent-Kolubara lignite. *Fuel Process. Technol.* **2012**, *95*, 1−7.
(36) Kong, Z.; Li, X.; Tian, J.; Yang, J.; Sun, S. Comparative study on the adsorption capacity of raw and modified litchi pericarp for removing Cu (II) from solutions. *J. Environ. Manage.* **2014**, *134*, 109−116.
(37) Freundlich, H. Over the adsorption in solution. *J. Phys. Chem. A* **1906**, *57*, 1100−1107.
(38) Lagergren, S. K. About the theory of so-called adsorption of soluble substances. *Sven. Vetenskapsakad. Handingarl* **1898**, *24*, 1−39.
(39) Blanchard, G.; Maunaye, M.; Martin, G. Removal of heavy metals from waters by means of natural zeolites. *Water Res.* **1984**, *18*, 1501−1507.
(40) Hevira, L.; Ighalo, J. O.; Zein, R. Biosorption of indigo carmine from aqueous solution by *Terminalia catappa* shell. *J. Environ. Chem. Eng.* **2020**, *8*, No. 104290.
(41) Tran, H. N.; You, S.-J.; Hosseini-Bandegharaei, A.; Chao, H.-P. Mistakes and inconsistencies regarding adsorption of contaminants from aqueous solutions: a critical review. *Water Res.* **2017**, *120*, 88−116.
(42) Chien, S.; Clayton, W. Application of Elovich equation to the kinetics of phosphate release and sorption in soils. *Soil Sci. Soc. Am. J.* **1980**, *44*, 265−268.
(43) Khan, A. A.; Singh, R. Adsorption thermodynamics of carbofuran on Sn (IV) arsenosilicate in H^+, Na^+ and Ca^{2+} forms. *Colloids Surf.* **1987**, *24*, 33−42.
(44) Maleki, M.; Moradi, O.; Tahmasebi, S. Adsorption of albumin by gold nanoparticles: Equilibrium and thermodynamics studies. *Arabian J. Chem.* **2017**, *10*, S491−S502.
(45) Sokić, M. D.; Marković, B.; Živković, D. Kinetics of chalcopyrite leaching by sodium nitrate in sulphuric acid. *Hydrometallurgy* **2009**, *95*, 273−279.
(46) Vilcáez, J.; Suto, K.; Inoue, C. Bioleaching of chalcopyrite with thermophiles: temperature−pH−ORP dependence. *Int. J. Miner. Process.* **2008**, *88*, 37−44.
(47) Mabusela, B.; Ojumu, T. V. *The Effect of Initial Solution pH on Surface Properties of Ferric Ion Precipitates Formed during Biooxidation of Ferrous Ion by Leptospirillum ferriphilum*; Solid State Phenomena, Trans Tech Publ, 2017; pp 403−407.

https://doi.org/10.1021/acsomega.1c03855
ACS Omega 2021, 6, 27984−27993